nanomaterials

MDPI

Article

Biosynthesis and Characterization of *Staphylococcus* sp. YRA-Derived Silver Nanoparticles with Antibacterial, Antibiofilm and Low Phytotoxic Effects

Yaleyvis Buelvas-Montes [1,2,3], Alfredo Montes-Robledo [1,3,4] and Rosa Baldiris-Avila [1,4,*]

1 Grupo de Investigación Microbiología Clínica y Ambiental, Facultad Ciencias Exactas y Naturales, Universidad de Cartagena, Cartagena 130001, Colombia; ybuelvas@unisinucartagena.edu.co (Y.B.-M.); amontesr@unicartagena.edu.co (A.M.-R.)
2 Facultad de Medicina Veterinaria y Zootecnia, Universidad de Córdoba, Montería 230001, Colombia
3 Grupo de Investigación GENOMA, Seccional Cartagena, Elías Bechara Zainúm, Universidad del Sinú, Cartagena 130001, Colombia
4 Facultad de Ciencias Exactas y Naturales, Universidad de Cartagena, Cartagena 130001, Colombia
* Correspondence: rbaldirisa@unicartagena.edu.co

Abstract

Silver nanoparticles were biosynthesized using the culture supernatant of *Staphylococcus* sp. YRA, a strain isolated from Colombian mining sediments. Synthesis was optimized at 1 mM $AgNO_3$, pH 7, 40 °C and 7 µg/mL extract, producing spherical, protein-capped AgNPs with primary sizes in the tens-of-nanometers range (~35–90 nm by SEM), while DLS indicated larger hydrodynamic diameters (~250–320 nm) consistent with aggregation in suspension (ζ-potential −16.6 mV). These nanoparticles remained stable over 6 months. Characterization by UV–Vis, SEM, AFM, EDS and FTIR confirmed extracellular protein-mediated reduction and capping. The AgNPs showed antibacterial activity against multidrug-resistant clinical isolates (*Staphylococcus aureus*, *Escherichia coli*, *Klebsiella pneumoniae*, *Salmonella bongori*, *Enterococcus* spp.), with inhibition zones of 8–16 mm at 400–1000 µg/mL. Biofilm formation was reduced by >50% at 700 µg/mL in both Gram-positive and Gram-negative strains. In *Phaseolus vulgaris* (*P. vulgaris*), low concentrations (5–100 µg/mL) increased growth and chlorophyll content, while 500 µg/mL caused moderate inhibition. FTIR analysis identified amide and thiol groups from bacterial enzymes as capping agents. These results suggest *Staphylococcus* sp. YRA as a bacterial platform for AgNPs production with antibiofilm activity against MDR pathogens and acceptable phytotoxicity profile for potential applications.

Keywords: *Staphylococcus* sp.; silver nanoparticles; phytotoxicity; antibacterial; antibiofilm

Check for updates

Academic Editors: Manolis Stratakis and Antonios Kelarakis

Received: 31 December 2025
Revised: 22 January 2026
Accepted: 16 February 2026
Published: 20 February 2026

Copyright: © 2026 by the authors. Licensee MDPI, Basel, Switzerland. This article is an open access article distributed under the terms and conditions of the Creative Commons Attribution (CC BY) license.

1. Introduction

Nanotechnology has developed rapidly since the 1980s and involves the manipulation of materials at the 1–100 nm scale, where size-dependent physicochemical properties emerge that are not typically observed in bulk materials [1,2]. These nanoscale features have enabled advances across scientific and industrial sectors, including agriculture and medicine. At the same time, the growing production of nanomaterials has raised questions regarding potential impacts associated with their manufacture, use, and disposal [3].

In addition to end-use concerns, synthesis routes have received increasing scrutiny. Conventional physical and chemical methods can require substantial energy input and may rely on hazardous reducing or stabilizing agents, motivating the development of greener alternatives [4]. Green synthesis approaches use biological molecules such as proteins,

polysaccharides, and antioxidants from plants and microorganisms to reduce and stabilize metal nanoparticles under milder conditions and with fewer harmful by-products [5,6]. Bacteria are particularly attractive platforms because they grow rapidly, adapt to diverse environments, and possess enzymatic systems and metal-tolerance mechanisms that can facilitate metal-ion reduction and nanoparticle stabilization [7,8].

Among metal-based nanomaterials, silver nanoparticles (AgNPs) have attracted considerable attention as antimicrobial agents in the context of multidrug-resistant (MDR) bacteria [9,10]. The growing burden of MDR infections is linked to extensive antibiotic use and misuse across clinical and non-clinical settings, which accelerates the selection and dissemination of resistant strains and reduces the effectiveness of conventional therapies. Beyond genetic resistance, treatment failure is also driven by bacterial lifestyles that further reduce antimicrobial susceptibility, particularly biofilm formation, which increases tolerance to antibiotics, disinfectants, and host defense mechanisms.

Biofilms are structured microbial communities embedded in an extracellular polymeric matrix that restricts antimicrobial penetration, creates heterogeneous microenvironments, and promotes phenotypic states associated with persistence. As a result, biofilm-associated infections can be difficult to eradicate and may recur despite antibiotic therapy and disinfection efforts. For this reason, strategies that interfere with early biofilm development particularly by limiting initial adhesion and matrix formation are increasingly viewed as valuable complements to conventional antibacterial approaches.

AgNPs are of interest because nanoscale features small size, high surface reactivity, and high surface-to-volume ratios, facilitate close contact with bacterial surfaces and enhance nano–bio interactions. Their antibacterial activity can involve multiple mechanisms, including interactions with the bacterial envelope, loss of membrane integrity, disruption of intracellular functions, and oxidative-stress-related effects, ultimately compromising cell viability through more than one pathway [9,10]. AgNPs can interact not only with bacterial cells but also with biofilm-associated components. During the early stages of biofilm development, reported antibiofilm effects include reduced initial adhesion and attenuation of extracellular polymeric substance (EPS) production, which can delay or limit biofilm establishment [11].

These outcomes have been linked to AgNP–EPS interactions, membrane perturbation, and oxidative-stress-related processes that impair bacterial attachment and early community stabilization [12]. Accordingly, assessing AgNPs for inhibition of biofilm formation, alongside planktonic antibacterial activity, is particularly relevant when testing against MDR isolates that readily adopt the biofilm lifestyle, because nanoparticle-based agents can act through multiple, concurrent interactions with both cells and matrix-related components rather than relying on a single antibiotic target [13]. Together, these considerations support evaluating AgNPs as a non-antibiotic antimicrobial approach that may complement conventional treatments and help reduce selection pressure associated with antibiotic-only strategies.

Alongside antimicrobial performance, the increasing use of AgNP-containing materials and the possibility of environmental release support considering concentration-dependent effects on plants and other organisms in the environment [14]. Despite their promising applications, AgNPs have raised concerns regarding potential environmental and phytotoxic effects, particularly because plants are among the first biological systems exposed to nanomaterials released into soils and water bodies [15]. Multiple studies report that AgNPs can be taken up by plants and influence physiological processes, with outcomes observed in germination, early seedling development, biomass, and photosynthetic pigment content; these responses depend strongly on nanoparticle size, surface chemistry, and exposure concentration [16]. Accordingly, plant-based assays offer a practical first-line

approach for screening phytotoxic responses and capturing dose-dependent stress signals in living tissues. *Phaseolus vulgaris* is frequently used in phytotoxicity screening because of its rapid germination, sensitivity to xenobiotic stressors, and agricultural relevance. Overall, such assays help place antimicrobial findings in a broader biological perspective and provide an initial indication of concentration ranges associated with minimal adverse effects [17].

This contribution focuses on the extracellular biosynthesis of AgNPs using *Staphylococcus* sp. YRA, a strain isolated from mining sediments in the Colombian Caribbean. The resulting AgNPs were characterized by UV–Vis spectroscopy, scanning electron microscopy (SEM), energy-dispersive X-ray spectroscopy (EDS), atomic force microscopy (AFM), ζ-potential, and Fourier-transform infrared spectroscopy (FTIR). Antibacterial and antibiofilm activities were evaluated against multidrug-resistant Staphylococcus aureus, *Escherichia coli*, *Klebsiella pneumoniae*, *Salmonella bongori*, *Enterococcus faecium*, and *Enterococcus faecalis*. In addition, phytotoxic effects were assessed using Phaseolus vulgaris seeds, a model species frequently used in phytotoxicity assays due to its sensitivity to xenobiotic agents and its capacity to exhibit either inhibitory or stimulatory responses depending on exposure conditions.

2. Materials and Methods

2.1. Isolation and Characterization of Staphylococcus sp. YRA

The bacterial strain *Staphylococcus* sp. YRA was isolated from sediment samples collected at a gold mining site in the district of San Martín de Loba (southern Bolívar, Colombia) by spread plating on nutrient agar and incubating until pure colonies were obtained [18]. Phenotypic characterization was carried out using standard microbiological and biochemical tests [19].

Genotypic identification was based on partial 16S rRNA gene sequencing. Genomic DNA was extracted with the DNeasy Blood & Tissue kit (Qiagen, Germantown, MD 20874, USA), and a ~1.5 kb 16S rRNA fragment was amplified using the universal primers 27F and 1492R, following the conditions described by Weisburg et al. [20]. PCR reactions (25 µL) contained 50 ng of template DNA, 10 pM of each primer, and DreamTaq PCR Master Mix (2×). Amplicons were checked on 1.5% agarose gels, purified, and sequenced by the Sanger method. The resulting sequences were compared with the NCBI (BLASTn) and EzBioCloud databases to determine the taxonomic affiliation of the strain, and the 16S rRNA gene sequence of *Staphylococcus* sp. YRA was deposited in GenBank (https://www.ncbi.nlm.nih.gov/genbank accessed on 1 December 2025). Phylogenetic analysis was performed in MEGA 12 using the neighbor-joining method, with evolutionary distances calculated by the maximum composite likelihood model and branch support assessed by 1000-replicate bootstrap analysis [21].

2.2. Extracellular Biosynthesis and Purification of AgNPs

To biosynthesize AgNPs, *Staphylococcus* sp. YRA was cultured in LB broth at 37 °C for 24 h [22]. The resulting cultures were centrifuged at 14,500 rpm for 15 min, and the bacterial supernatant was extracted and filtered twice through a 0.22 µm syringe filter [23]. The total protein content was determined using Bradford's method with 10–100 µg of bovine serum albumin as a standard [24].

The screening of AgNPs biosynthesis followed published procedures with minor modifications [25]. Cell-free extracts were mixed with aqueous $AgNO_3$ to a final concentration of 1 mM. The reaction mixture was incubated at 40 °C under static conditions for 160 h, and nanoparticle formation was preliminarily monitored by visual color change (colorless to brown) and confirmed by UV–Vis spectroscopy (SPR band). The synthesis controls were

included: (i) cell-free extract without $AgNO_3$ (negative control/blank), (ii) $AgNO_3$ solution without bacterial supernatant (ionic precursor control), and (iii) supernatant processed without the protein-containing fraction (protein-free control) [26,27].

Optimizing the Biosynthesis of AgNPs by *Staphylococcus* sp. YRA

To optimize the synthesis of nanoparticles, several reaction parameters were investigated, including concentration of metal ions (0.5, 0.7, 1, 2, 3, 4, 5 mM), temperature (20, 30, 40, 50, 60, 70, 80 °C), light/dark conditions (0, 5, 15, 30, 45, 60 min), cell-free extract concentration (0, 1, 2, 3, 5, 7, 10 µg/mL), pH (1, 2, 3, 4, 5, 6, 7, 8, 9, 10), culture age (6, 12, 18, 24, 48, 72, 96, 120 h), and time (0, 15 h) [28]. These parameters were investigated using a one-factor optimization approach in LB broth; spectrophotometry was used to monitor all tests, and the stability of the products was monitored after 15, 30, 60, 120, 180 days [29]. Once the optimal conditions were determined, characterization analyses were carried out. To identify the biotransformation reactions of Ag^+ to Ag^0, Mohr's titrimetric method was used. The method involved using 10 mL of 1 mM KCl solution, 0.5 mL of 0.25 M K_2CrO_4 indicator, the precursor $AgNO_3$ solution, and the colloidal solution of AgNPs as titrant. An incomplete reduction was indicated by the presence of a brick-red precipitate of Ag_2CrO_4, while the absence of precipitate indicated complete reduction [30].

2.3. Characterization of Biosynthesized AgNPs

The biosynthesized AgNPs were characterized using UV–Visible spectrometry, scanning electron microscopy (SEM), atomic force microscopy (AFM), dynamic light scattering, surface zeta potential, and Fourier-transform infrared (FT-IR) analysis [31].

2.3.1. Ultraviolet–Visible Spectrometry (UV–Vis)

To confirm the formation of AgNPs, UV–Vis analysis was performed by placing 150 µL of the aqueous solution of AgNPs on 96 flat-bottom transparent polystyrene plates and recording an absorption spectrum within the wavelength range of 200–800 nm, with a wavelength step size of 10 nm at a temperature of 25 °C [13]. The appearance of a surface plasmon resonance (SPR) band in the 420–450 nm region was used as an optical indicator consistent with AgNPs formation. A cell-free filtrate without silver nitrate was used as a blank sample for control purposes.

2.3.2. Scanning Electron Microscopy (SEM)

The morphology, size, and shape of AgNPs were evaluated using scanning electron microscopy (SEM TESCAN Brno, s.r.o., based in the Czech Republic). SEM micrographs were used to confirm nanoparticle formation through the visualization of nanoscale structures and to evaluate particle morphology as well as the presence of aggregation. AgNPs were prepared by washing with sterile deionized water, fixed with 2.5% glutaraldehyde, and dry samples were covered with a layer of colloidal gold and observed in the scanning electron microscope [32].

2.3.3. Atomic Force Microscopy (AFM)

To analyze AgNPs using atomic force microscopy (AFM Asylum Research (Oxford Instruments Asylum Research), Santa Barbara, California, USA.), the solution was spin-coated onto a glass substrate and air-dried at room temperature for 12 h. AFM height and phase/topography images were analyzed to confirm nanoparticle presence as individual nanoscale features and to determine size-related parameters. Multiple different areas of the sample were scanned to obtain a representative analysis of the AgNPs [32].

2.3.4. Dynamic Light Scattering (DLS) and Surface Zeta Potential (SZP)

Surface zeta potential and dynamic light scattering of the AgNPs was determined using a Zetasizer Nano ZS (Malvern Instruments Ltd., Malvern, United Kingdom.) equipped with a surface zeta potential cell and 5 mM citrate buffer containing polystyrene latex tracer particles (100 ppm). DLS data were used to obtain the Z-average hydrodynamic diameter and polydispersity index (PDI) as indicators of particle size distribution and colloidal homogeneity. SZP measurements were used to evaluate colloidal stability. SZP values were calculated from at least three independent measurements and reported as mean ± standard deviation [33].

2.3.5. Fourier-Transform Infrared (FT-IR) Analysis

The supernatant and synthesized AgNPs were analyzed by FT-IR (ATR mode) (Thermo Fisher Scientific, Waltham, MA, USA) by directly applying each sample onto the diamond crystal. FT-IR profiles were compared between supernatant and AgNPs samples to detect band shifts, intensity changes, or the appearance/disappearance of peaks, which were interpreted as evidence of biomolecules adsorbed on the nanoparticle surface. Spectra were background-corrected (air) and recorded in the 4000–400 cm^{-1} range [34].

2.4. Antibacterial and Antibiofilm Activity

2.4.1. Tested Pathogenic Organisms

To determine the antibacterial and antibiofilm efficacy of the synthesized nanoparticles, multidrug-resistant isolates from clinical specimens and food sources were selected. All isolates were confirmed by partial 16S rRNA gene sequencing prior to downstream assays [19]. Genomic DNA was extracted from phenotypically confirmed isolates using the GeneJET Genomic DNA Purification Kit (Thermo Fisher Scientific, Waltham, MA, USA) according to the manufacturer's instructions and used for subsequent PCR-based analyses. Strain sources, biofilm production and morphotypes, together with key phenotypic/genotypic markers, are summarized in the Supplementary Material (Table S2). Clinical & Laboratory Standards Institute (CLSI) interpreted antimicrobial susceptibility profiles are provided in the Supplementary Material (Table S3).

2.4.2. Antibacterial Activity

The antibacterial activity of AgNPs was evaluated using an agar well diffusion assay. Overnight cultures in Mueller–Hinton broth (MHB) were adjusted to 0.5 McFarland and spread onto Mueller–Hinton agar (MHA) plates. Wells were punched in the agar and filled with AgNPs suspensions (final concentrations 10–1000 µg/mL). Plates were incubated at 37 °C for 24 h, and inhibition-zone diameters were measured [35]. All assays were performed in triplicate and are reported as mean values. CLSI guidelines were followed for inoculum standardization and incubation conditions (CLSI, M02/M07). The antibacterial assays were conducted against MDR clinical and food-derived isolates (including *Staphylococcus aureus*, *Escherichia coli*, *Klebsiella pneumoniae*, *Salmonella bongori*, and *Enterococcus* spp.). Reference strains were included as quality controls (*E. coli* ATCC 25922, *E. coli* O157:H7 ATCC 35150, *Enterococcus faecalis* ATCC 29212, *K. pneumoniae* ATCC 700603, *Salmonella typhimurium* ATCC 13311, and *S. aureus* ATCC 25923).

2.4.3. Antibiofilm Activity

To assess the impact of biosynthesized AgNPs on biofilm formation, we performed a modified microtiter plate assay based on crystal violet staining of surface-attached cells [36]. Initially, isolates were screened for biofilm-forming capacity and colony morphotypes were determined on BHI-based Congo red agar supplemented with sucrose. Morphotypes were

categorized as rdar, bdar, pdar, or saw based on colony appearance after 24 h of incubation, as previously described [37]. Biofilm formation was quantified using the microtiter plate assay and classified as non-biofilm producer (OD $\leq$ ODc), weak biofilm producer (OD > ODc and $\leq 2 \times$ ODc), moderate biofilm producer (OD > $2 \times$ ODc and $\leq 4 \times$ ODc), and strong biofilm producer (OD > $4 \times$ ODc) according to Stepanović et al., 2007 [38].

To evaluate antibiofilm activity, sterile 96-well microtiter plates were filled with 180 µL of fresh LB broth. A 20 µL mixture (1:1) containing 10 µL of overnight bacterial culture adjusted to a 0.5 McFarland standard and 10 µL of AgNPs suspension was added to each well to obtain final AgNPs concentrations ranging from 100 to 1000 µg/mL. Plates were incubated at 37 °C for 24 h. After incubation, wells were gently washed three times with 200 µL of sterile deionized water to remove non-adherent cells, air-dried for 30 min, and stained with 0.5% crystal violet for 30 min. Plates were then washed five times with sterile deionized water, and the bound dye was solubilized by adding 200 µL of an 80% ethanol/20% acetone mixture followed by incubation for 15 min. Absorbance was measured at 492 nm [39]. Untreated microbial controls (no AgNPs) were processed under the same conditions. As a positive control, *Klebsiella pneumoniae* ATCC 700603 was included. All experiments were performed in triplicate, and the percentage of biofilm activity inhibition (%BAI) was calculated as follows:

$$\left[\%BAI = \frac{(A_{492}\ of\ non\text{–}treated\ control\ cells) - (A_{492}\ of\ cells\ treated\ with\ AgNPs)}{A_{492}\ of\ non\text{–}treated\ control\ cells}\right] \times 100 \quad (1)$$

The average values for minimum inhibitory concentration (MIC), minimum bactericidal concentration (MBC), and biofilm inhibition were determined based on three separate experiments.

2.5. Phytotoxicity Test of AgNPs in Phaseolus vulgaris

Before conducting phytotoxicity tests, *P. vulgaris* seeds were subjected to disinfection using a 1–5% sodium hypochlorite solution for 15 min, followed by five rinses with sterile water, following the procedure proposed by Yang et al. [40]. The seed germination test was performed under aseptic conditions in glass Petri dishes, with a layer of filter paper (140 mm Whatman™ Merck KGaA, Darmstadt, Germany) placed at the bottom of each dish. Each experimental unit consisted of 10 seeds treated with different concentrations of AgNPs solution (0, 5, 50, 100, and 500 µg/mL) or distilled water (control), with three replicates for each concentration. The experiment was conducted in triplicate. After sowing, the seeds were incubated in the dark at a temperature of 25 ± 1 °C. The number of germinated seeds was recorded daily, with the criterion for germination being the emergence of the radicle (>1 mm), as described by Salvatore et al. [41].

Once the seeds had germinated, seedlings were transferred from the Petri dishes to sterile 0.8% (*w*/*v*) agar base (bacteriological agar) prepared with sterile distilled water and supplemented with AgNPs at 0, 5, 50, 100, and 500 µg/mL in each glass flask, following the protocols of Naraginti et al. [42] and López-Escamilla et al. [43]. Control experiments were included with negative control (Control −) was included using sterile Milli-Q water without AgNPs (0 µg/mL). In addition, a positive control (Control +) was prepared using 0.05 M zinc sulfate heptahydrate ($ZnSO_4 \cdot 7H_2O$) to provide a reference phytotoxic stress condition. Both controls were incubated and handled identically to the AgNPs treatments. After sowing, the seeds were incubated at a temperature of 25 ± 1 °C with a photoperiod of 12 h of darkness and 12 h of light for 15 days, following the method of Gupta et al. [44]. The experiments were conducted in triplicate, and the data are presented as the average ± standard error in this study.

The chlorophyll a and b, as well as the total chlorophyll (a + b) content, were determined using the following equations, where V represents the volume of the leaf extract

(in mL) and FW indicates the fresh weight of the leaf sample (in g). The determination of chlorophyll and carotenoid contents followed the procedure outlined by Sumanta et al. [45]. Specifically, 100 mg of leaf samples were ground with a pre-chilled mortar and pestle in 10 mL of 80% acetone maintained at a low temperature. The resulting pulp was then centrifuged at 8000 g and 4 °C for 10 min. The absorbance of the supernatant was measured at 470, 646.8, and 663.2 nm using a UV–Vis spectrophotometer, with 80% acetone as the blank, to calculate the chlorophyll and carotenoid contents. The amounts of chlorophyll a, chlorophyll b, total chlorophyll (a + b) and carotenoids were calculated using the following formulas:

$$Chl\ a\ (\mathrm{mg/g}) = \frac{(12.25 \times Abs_{663.2} - 2.79 \times Abs_{646.8}) \times V}{1000 \times FW} \quad (2)$$

$$Chl\ b\left(\frac{\mathrm{mg}}{\mathrm{g}}\right) = \frac{(21.5 \times Abs_{648.8} - 5.1 \times Abs_{663.2}) \times V}{1000 \times FW} \quad (3)$$

$$Chl\ a + b\ (\mathrm{mg/g}) = \frac{(7.15 \times Abs_{663.2} - 18.71 \times Abs_{646.8}) \times V}{1000 \times FW} \quad (4)$$

$$Carotenoids\left(\frac{\mathrm{mg}}{\mathrm{g}}\right) = \frac{(1000 \times Abs_{470} - 1.82 \times Chl\ a - 85.02 \times Chl\ b) \times V}{198 \times 1000 \times FW} \quad (5)$$

The study estimated the toxic effects of different concentrations of AgNPs on *Phaseolus vulgaris* seedlings, both treated and untreated. The evaluation of phytotoxicity was based on seed germination, root and shoot length, biochemical parameters, and enzymatic activity, as per Roy et al. [46]. The percentage of relative seed germination (GRS %), relative root growth (CRR %), relative hypocotyl growth (CRH %) and germination index (IG %) [47] were evaluated according to Table 1.

Table 1. Equations for each variable in the phytotoxicity assay using *P. vulgaris* seeds.

Variable	Equation
GRS	$GRS(\%) = \frac{Number\ of\ germinated\ seeds\ in\ negative\ control}{Number\ of\ germinated\ seeds\ in\ positive\ control} \times 100\%$
CRR	$CRR(\%) = \frac{Average\ root\ length\ in\ negative\ control}{Average\ root\ length\ in\ evaluated\ sample} \times 100\%$
CRH	$CRH(\%) = \frac{Average\ hypocotyl\ length\ in\ negative\ control}{Average\ hypocotyl\ length\ in\ evaluated\ sample} \times 100\%$
IG	$IG(\%) = \frac{GRS \times CRR}{100}$

2.6. Statistical Data Analysis

All experiments were performed in triplicate, and the reported results represent the mean ± standard error. Statistical analysis was conducted using Prism 7.02 GraphPad Software [48]. The parametric or non-parametric nature of the data was determined using the Shapiro-Wilk normality test ($p > 0.05$). For parametric data, a one-way analysis of variance (ANOVA) followed by Dunnett's test was used for comparisons against the controls. For non-parametric data, the Kruskal-Wallis test followed by Dunn's test was employed for comparisons against the controls.

3. Results and Discussion

3.1. Isolation of Staphylococcus sp. Strain YRA

The YRA strain was identified as Gram-positive cocci arranged in clusters, catalase-positive, coagulase-negative, urease-positive and non-motile, features consistent with coagulase-negative *Staphylococcus* species. In carbohydrate utilization tests, it produced acid from glucose, lactose, maltose, mannitol and arabinose, a pattern typically described

for environmental species. These characteristics clearly distinguished strain YRA from coagulase-positive species such as *Staphylococcus aureus* [18].

Analysis of the 16S rRNA gene sequence supported the phenotypic identification. In the phylogenetic tree constructed from partial 16S rRNA sequences, *Staphylococcus* sp. strain YRA (PX759760) clustered in a single clade together with *Staphylococcus xylosus* (D83374) and two sequences of *Staphylococcus saprophyticus* (NR114090 and D83371), and was clearly separated from the clades including *Staphylococcus arlettae* (KM659860), *S. aureus* (D83353), *Staphylococcus hominis* (KF574083) and *Staphylococcus pasteuri* (MH360978), with *Escherichia coli* (NR024570) used as an outgroup (Figure 1). This topology indicates a closer evolutionary relationship of YRA to coagulase-negative *Staphylococcus* species typically associated with environmental and animal niches, consistent with its isolation from mining sediments.

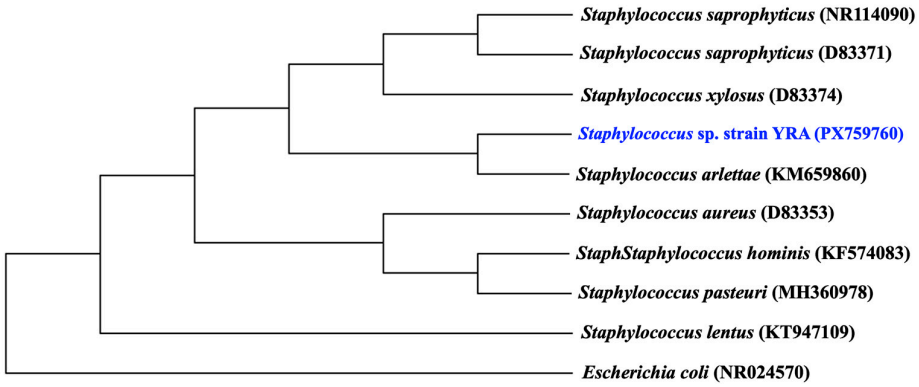


Figure 1. Neighbor-joining phylogenetic tree based on 16S rRNA gene sequences, showing the position of *Staphylococcus* sp. YRA (GenBank accession PX759760).

3.2. Synthesis and Purification of AgNPs

The formation of AgNPs was first evidenced by the visible color change in the reaction mixture, which shifted from colorless to brown (Figure 2). In contrast, the control reactions (cell-free extract without $AgNO_3$ and $AgNO_3$ without supernatant) did not show a comparable color change. This color development is attributed to the excitation of surface plasmon vibrations in silver nanoparticles and is widely used as a convenient spectroscopic signature of AgNPs formation [22,23]. After synthesis, the UV–Vis spectrum of the brown colloidal dispersion was recorded in the 300–800 nm range. The spectrum displayed an SPR feature centered at ~420–430 nm; because AgNPs SPR typically occurs between 400 and 450 nm, the band observed in Figure 2 supports successful nanoparticle synthesis.

With respect to the effect of reaction time on AgNPs production, a positive correlation was observed between absorbance intensity and the incubation time of silver nitrate with the bacterial supernatant, indicating progressive nanoparticle formation. For synthesis optimization (Figure 2a), extracellular protein extract (7 μg/mL) was added to $AgNO_3$ solutions under standardized conditions (1 mM $AgNO_3$, pH 7, 40 °C). Among the concentrations evaluated, 0.5 mM $AgNO_3$ promoted rapid initial SPR development, indicating efficient early-stage Ag^+ reduction; however, the total amount of AgNPs formed under this condition was limited, and the resulting colloid exhibited reduced stability, as evidenced by visible precipitation during storage [34]. In contrast, 1 mM $AgNO_3$ yielded a more intense and sustained SPR signal, consistent with improved nanoparticle yield and colloidal stability [49].

When the $AgNO_3$ concentration was increased to 1 mM, a more intense brown color and improved colloidal stability were obtained, whereas concentrations above 3 mM led to turbid, grayish suspensions with poor stability. Regarding pH, an immediate color change was observed at pH 3 and 13, yielding whitish-violet and yellow solutions, respectively, but

the corresponding UV–Vis spectra did not display well-defined plasmon bands. At pH 5, 7 and 9, the spectra were similar and partially overlapped, indicating limited nanoparticle formation under these conditions [28].

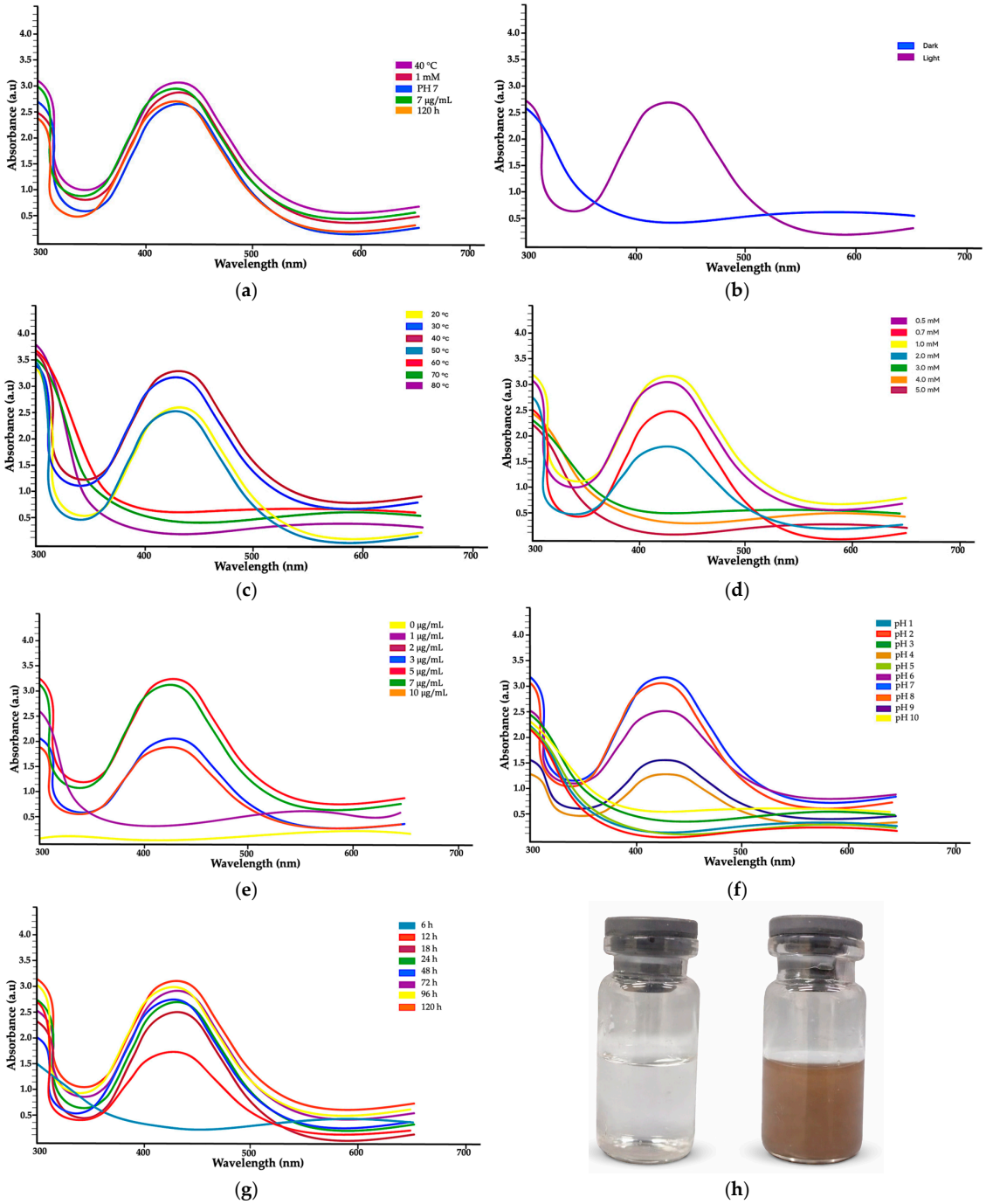


Figure 2. Optimization of synthesis parameters for AgNPs using *Staphylococcus* sp. YRA. (**a**) UV–Vis spectra obtained under the selected optimal level of each parameter. (**b**) Effect of light/dark conditions. (**c**) Effect of temperature. (**d**) Effect of $AgNO_3$ concentration. (**e**) Effect of cell-free extract concentration. (**f**) Effect of pH. (**g**) Effect of culture age. (**h**) Silver nitrate solution (1 mM) before (left) and after (right) exposure to the culture supernatant.

The influence of HCl and NaOH on the synthesis was also examined using Milli-Q water as solvent. Negligible AgNPs formation was detected at pH 5, 7 and 9, while the responses at pH 3 and 13 were maintained, suggesting that NaOH can act as a chemical reducing agent for silver ions in the absence of bacterial components. On this basis,

pH 7 was selected as the optimal reaction condition to avoid interference from HCl or NaOH and to ensure that AgNPs formation was mainly driven by bacterial extracellular molecules [50].

To assess the completeness of Ag^+ conversion by the extracellular components, NaCl was added to the final reaction mixture. The absence of a white AgCl precipitate suggested that free silver ions were not detectable under these conditions [26]. Consistently, the Mohr titrimetric method applied to the AgNPs colloid synthesized with the bacterial supernatant did not yield the characteristic reddish complex, supporting extensive conversion of Ag^+. Synthesis controls further supported the biosynthetic origin of the nanoparticles, $AgNO_3$ alone and cell-free extract without $AgNO_3$ did not develop the characteristic brown coloration or an SPR band, and the protein-free supernatant fraction did not show an SPR signal. In preliminary trials, non-filtered supernatant/medium controls led to visible precipitation and poorly defined spectra, consistent with matrix-driven salt formation and/or incomplete conversion under non-optimized conditions; therefore, all synthesis reactions used filtered cell-free extract to improve reproducibility and minimize interfering components.

3.3. Physicochemical and Morphological Characterization of Biosynthesized AgNPs

Scanning electron microscopy and atomic force microscopy showed predominantly quasi-spherical AgNPs with a polydisperse size distribution and a clear tendency to form aggregates (Figure 3). Based on the SEM micrographs, the apparent primary particle diameters were in the tens-of-nanometers range (approximately ~35–90 nm for well-resolved particles), while larger clustered structures were also observed at lower magnification. AFM topography further supported nanoscale features consistent with biogenic, surface-capped particles [51].

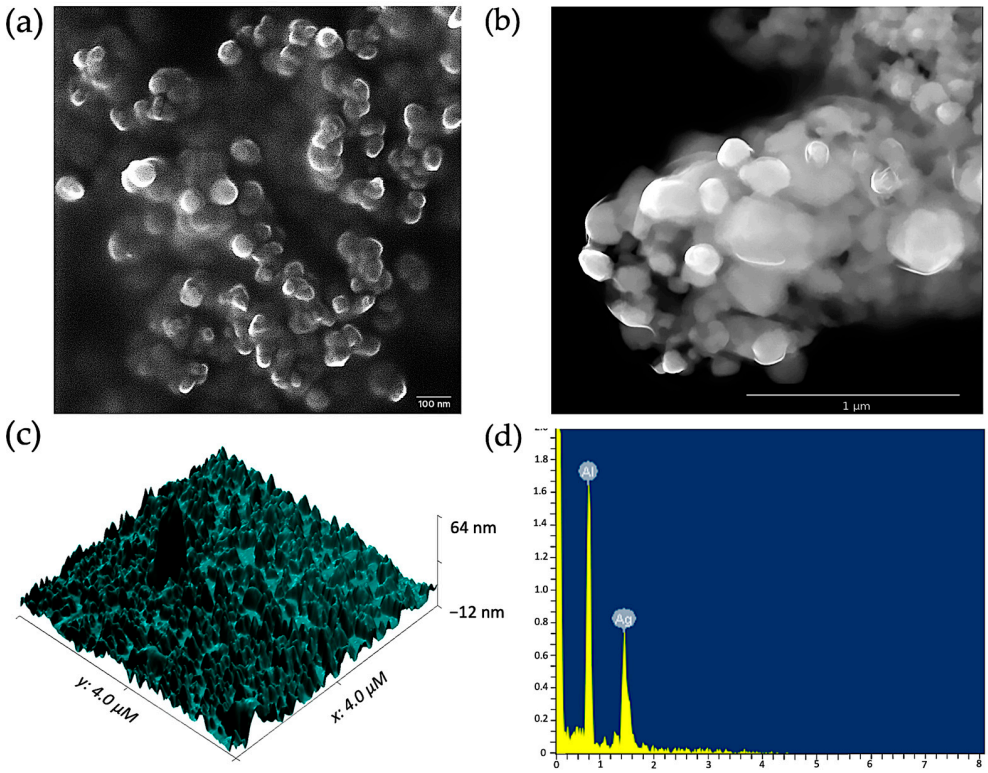


Figure 3. Characterization of biosynthesized AgNPs. (**a**) High-magnification SEM micrograph showing primary AgNPs (scale bar: 100 nm). (**b**) Lower-magnification SEM micrograph showing aggregation (scale bar: 1 µm). (**c**) AFM 3D topography image. (**d**) EDS spectrum acquired from AgNPs confirming the presence of Ag.

In aqueous suspension, dynamic light scattering showed a hydrodynamic Z-average diameter of 319.9 nm (PDI = 0.402), with a single main population centered at 249.7 nm (100% intensity), indicating the formation of colloidal aggregates larger than the primary cores. The surface zeta potential was −16.6 mV at 25 °C, with an electrophoretic mobility of −1.301 μm·cm/V·s and a conductivity of 0.0432 mS/cm, values consistent with a moderately negative surface charge and intermediate colloidal stability, below the ±30 mV threshold usually associated with highly stable colloidal dispersions [52].

These results are relevant because both the morphology and the size of AgNPs strongly influence their physicochemical behavior and, consequently, their potential applications, particularly in biomedicine and nanotoxicology. AgNPs in the tens-of-nanometers range can interact with cell membranes, favoring adsorption to the membrane surface and, in some cases, internalization, which may lead to limited membrane damage but also enables their use as carriers in drug delivery systems by facilitating cellular uptake [53]. The larger hydrodynamic diameter compared with SEM is expected for biogenic AgNPs due to agglomeration and the presence of a biomolecular corona in aqueous suspension. Therefore, microscopy-based sizes reflect the dry primary particles, whereas DLS reflects the colloidal/solvated state of the system.

EDS analysis showed a characteristic Ag signal around 3 keV, confirming the presence of silver in the analyzed region (Figure 3d). EDS is an elemental-composition technique and does not provide information on oxidation state or plasmonic behavior. In this study, surface plasmon resonance (SPR) was evidenced by UV–Vis spectroscopy through the absorption band in the 420–450 nm range, which is consistent with AgNPs formation [25]. A minor aluminum signal was attributed to the sample holder/substrate. Taken together, microscopy confirmed nanoscale, predominantly spherical particles, whereas DLS reflected larger hydrodynamic diameters in suspension due to aggregation/corona effects. Spherical AgNPs can exhibit enhanced antibacterial performance compared with anisotropic morphologies, partly due to increased surface contact with bacterial cells [54].

The FT-IR spectra of the bacterial cell-free extract (red) and the biosynthesized AgNPs (blue) are shown in Figure 4. The extract spectrum displayed bands at 3428, 2921, 1643, 1593 and 1384 cm^{-1}, which can be assigned to O–H/N–H stretching, aliphatic C–H stretching, and amide-related vibrations of proteins and other extracellular biomolecules [27]. In the AgNPs spectrum, the main bands at 3428 and ~2912 cm^{-1} were retained, while changes in the amide region (around 1633–1515 cm^{-1}) and the ~1036 cm^{-1} region (C–N/C–O vibrations) were observed, consistent with the involvement of proteinaceous components in nanoparticle reduction and surface capping [55]. Weak features around 2360–2315 cm^{-1} can arise from atmospheric CO_2 in FT-IR measurements and were not interpreted mechanistically. Overall, the FT-IR profiles support those extracellular biomolecules—particularly proteins/enzymes—participate as reducing and stabilizing agents during AgNPs biosynthesis.

AgNPs biosynthesis has frequently been attributed to enzymatically assisted Ag^+ reduction mediated by extracellular or cell-associated oxidoreductases (including NADH-dependent nitrate reductase and related redox enzymes), followed by capping/stabilization by biomolecules present in the supernatant [5,6,8]. The physicochemical stability of the AgNPs suspensions was monitored during storage by UV–Vis spectroscopy, assessing the persistence and shape of the surface plasmon resonance (SPR) band over time. The retention of a well-defined SPR profile after 6 months is consistent with sustained colloidal stability and supports the presence of an effective protein-based capping layer. Although the ζ-potential magnitude suggests only moderate electrostatic stabilization, FTIR indicated protein/thiol-containing capping agents that may provide steric stabilization, which could explain the observed colloidal stability over storage. At the same time, the moderate

ζ magnitude and the DLS/PDI values indicate aggregation in suspension, which may reduce effective bioavailability and contribute to the relatively high concentrations required to achieve measurable inhibition zones [56].

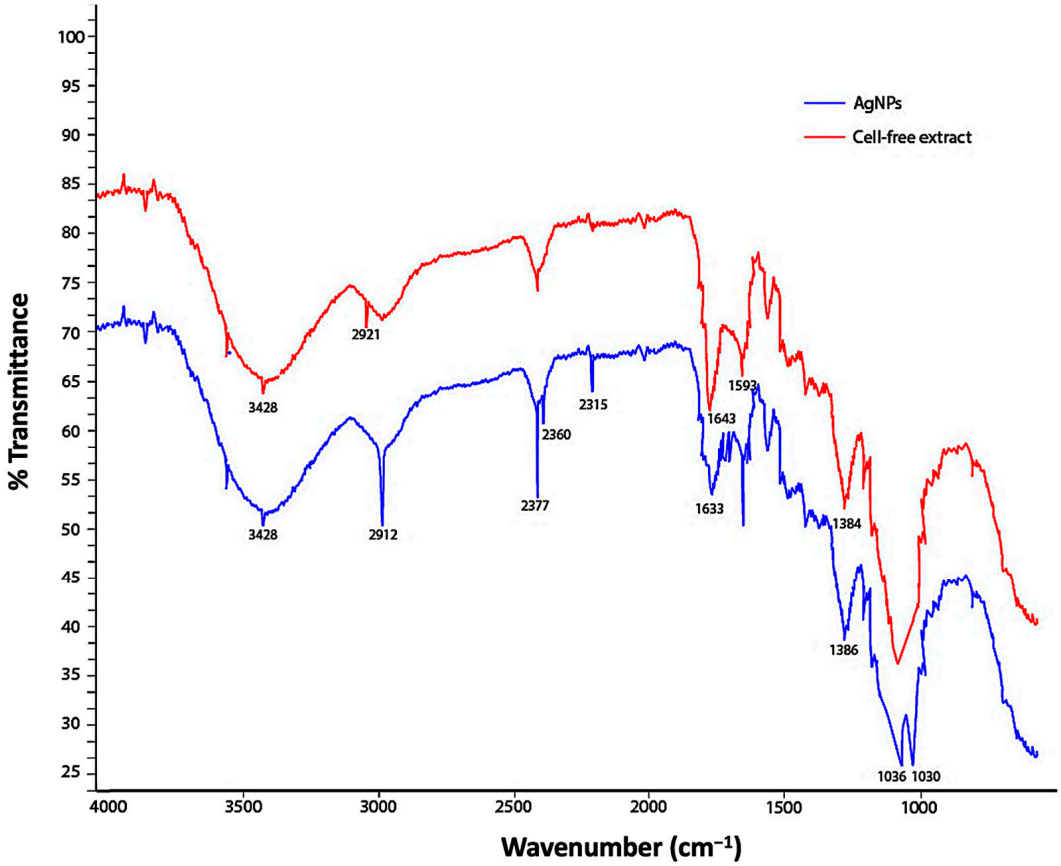


Figure 4. FT-IR spectra of the bacterial cell-free extract (red) and biosynthesized AgNPs (blue). Major bands are labeled (cm^{-1}). Bands in the 3428–2912 cm^{-1} region are consistent with O–H/N–H and aliphatic C–H stretching, while signals in the 1643–1515 cm^{-1} region correspond to amide I/amide II vibrations, supporting the involvement of proteinaceous extracellular components in AgNPs synthesis and capping.

NP synthesis involves Ag^+ bioreduction mediated by extracellular redox-active biomolecules, including oxidoreductases, which can transfer reducing equivalents to Ag^+ and promote nucleation and growth of Ag^0 nanoparticles [23]. The physicochemical stability of the AgNPs suspensions was monitored during storage by UV–Vis spectroscopy, assessing the persistence and shape of the surface plasmon resonance (SPR) band over time. The retention of a well-defined SPR profile after 6 months is consistent with sustained colloidal stability and supports the presence of an effective protein-based capping layer. Although the ζ-potential magnitude suggests only moderate electrostatic stabilization, FTIR indicated protein/thiol-containing capping agents that may provide steric stabilization, which could explain the observed colloidal stability over storage. At the same time, the moderate ζ magnitude and the DLS/PDI values indicate aggregation in suspension, which may reduce effective bioavailability and contribute to the relatively high concentrations required to achieve measurable inhibition zones [56]. These observations reinforce the contribution of extracellular proteins/enzymes as both reducing and capping components in biogenic AgNPs formation, consistent with reports describing enzyme-assisted synthesis and protein-mediated stabilization in bacterial systems [23,25].

3.4. Antibacterial Activity of Biosynthesized AgNPs

The biosynthesized AgNPs inhibited both Gram-negative and Gram-positive bacteria in a concentration-dependent manner. One-way ANOVA did not show significant overall differences among treatments and strains at $\alpha = 0.05$, whereas Tukey's post hoc test revealed significant differences between treatments for *E. coli* and *K. pneumoniae* ($p = 0.0402$), indicating that inhibition zones increased with AgNPs concentration. To provide a quantitative overview of the dose–response, inhibition-zone diameters obtained at each AgNPs concentration are reported in Table 2. No detectable inhibition halos were observed below 400 µg/mL for most strains, except for *E. coli* (detectable activity at 400 µg/mL) and *S. aureus* (detectable activity at 600 µg/mL). Overall, Gram-negative isolates tended to respond at lower concentrations than several Gram-positive isolates, which is consistent with previous reports showing higher apparent sensitivity of Gram-negative bacteria to AgNPs exposure [9–11].

Table 2. Antibacterial activity of AgNPs (inhibition zone diameters, mm).

Strain	[400]	[500]	[600]	[700]	[800]	[900]	[1000]
E. coli	8.23 ± 0.1	8.96 ± 0.1	10.7 ± 0.2	12.20 ± 0.0	13.74 ± 0.4	14.40 ± 0.1	16.35 ± 0.2
S. bongori	-	-	-	8.33 ± 0.3	8.37 ± 0.2	9.17 ± 0.1	9.25 ± 0.0
E. faecium	-	-	-	9.11 ± 0.1	10.0 ± 0.4	12.1 ± 0.2	12.9 ± 0.1
E. faecalis	-	-	-	9.30 ± 0.2	10.7 ± 0.1	11.87 ± 0.1	13.1 ± 0.3
S. aureus	-	-	7.56 ± 0.1	7.90 ± 0.1	8.66 ± 0.4	10.17 ± 0.1	11.2 ± 0.3
K. pneumoniae	-	-	-	-	8.11 ± 0.1	8.88 ± 0.1	9.78 ± 0.2

Differences among strains are expected because agar diffusion outcomes depend not only on intrinsic susceptibility but also on particle dispersion and mobility within the agar matrix [35]. In biogenic systems, protein-based capping and colloidal aggregation can reduce effective diffusion, shifting measurable inhibition halos toward higher applied concentrations. In this context, the requirement for relatively high AgNPs concentrations to generate clear halos is consistent with aggregation in suspension, which can limit the fraction of freely dispersed particles available to interact with cells at the agar–bacteria interface [56]. Despite this limitation, the progressive increase in inhibition-zone diameters with concentration—particularly for *E. coli*, *E. faecalis*, and *E. faecium*—supports a genuine dose–response relationship rather than an artifact.

Several studies have reported antibacterial activity of biogenic AgNPs against diverse pathogens, including *E. coli* and *P. aeruginosa*, with enhanced activity often linked to smaller particle size and higher specific surface area [57]. These effects are commonly interpreted considering bacterial envelope structure, Gram-negative bacteria possess a thinner peptidoglycan layer and an outer membrane that can facilitate interactions with AgNPs and silver species, promoting membrane destabilization and loss of integrity [58]. Beyond membrane damage, AgNPs may also contribute to oxidative-stress-related mechanisms, including reactive oxygen species generation associated with oxidative dissolution of silver, which can promote protein dysfunction and oxidative damage to DNA and other macromolecules [58]. Taken together, the antibacterial profiles observed here are consistent with the multi-target activity widely described for AgNPs, with efficacy modulated by particle concentration and colloidal state, as well as by species-specific cell-envelope properties [57,58].

3.5. Antibiofilm Activity of Biosynthesized AgNPs

All tested strains formed biofilms with varying intensities, consistent with their aggregative morphotypes on Congo red agar and their ability to persist under environmental stress and antimicrobial exposure [59,60]. Because biofilms are embedded in an extra-

cellular polymeric substance (EPS) matrix, they often exhibit increased tolerance compared to planktonic cells, making biofilm inhibition a relevant endpoint for evaluating antimicrobial nanomaterials.

AgNPs exposure reduced biofilm biomass in a dose-dependent manner. At 700 µg/mL, AgNPs produced >50% reduction in biofilm biomass for moderate/strong biofilm-forming strains, whereas lower concentrations were sufficient for certain isolates (400 µg/mL for *E. coli* and 600 µg/mL for *S. aureus*), indicating strain-dependent sensitivity. Comparable antibiofilm trends have been reported for AgNPs produced via biological routes, supporting the broader potential of AgNPs as anti-adhesion/anti-biofilm agents [11]. Concurrently, recent materials-based antimicrobial strategies emphasize the importance of surfaces and nano-enabled interfaces that reduce initial attachment and biofilm persistence, reinforcing the relevance of evaluating antibiofilm performance alongside planktonic inhibition [60]. Biofilm inhibition by AgNPs is presented for Gram-negative isolates (Figure 5) and Gram-positive isolates (Figure 6).

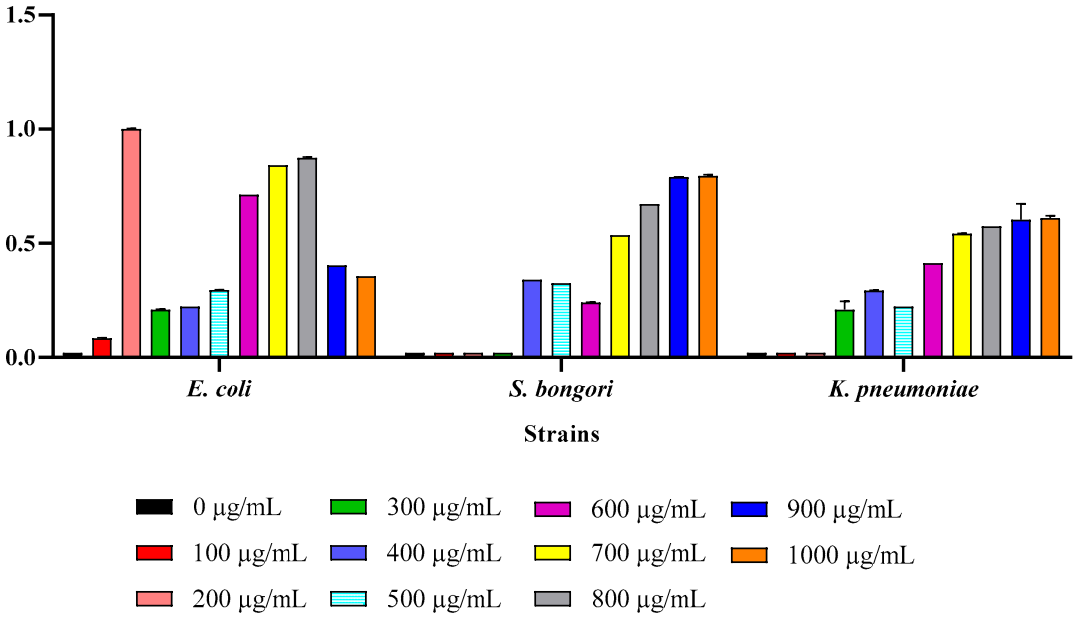


Figure 5. Effect of AgNPs on antibiofilm activity in Gram-negative bacterial strains.

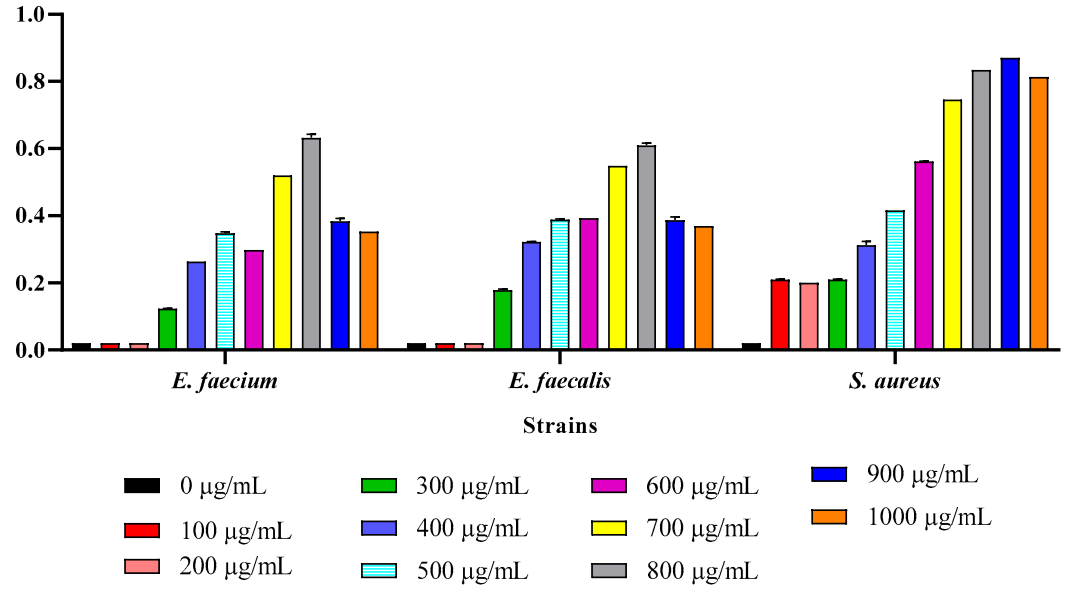


Figure 6. Effect of AgNPs on antibiofilm activity in Gram-positive bacterial strains.

Mechanistically, AgNPs can act at multiple stages of biofilm development. During early stages, nanoparticles may reduce initial attachment by altering cell–surface interactions and by interfering with EPS components that stabilize adhesion and microcolony formation. During maturation, AgNPs and silver species can diffuse into the matrix, perturb biofilm architecture, and reduce the viability of embedded cells, consistent with multifactorial antibiofilm activity linked to EPS interactions, membrane perturbation, and oxidative-stress-related effects [61]. In this study, the need for higher concentrations to achieve strong inhibition in some isolates is consistent with the protective nature of the EPS matrix and with aggregation in suspension, which may reduce the effective dose delivered to the biofilm interface [56]. Overall, the observed reductions across both Gram-negative and Gram-positive biofilms support the potential of these biosynthesized AgNPs as anti-biofilm agents, while also motivating future work using surface-relevant models and combined treatments to explore whether antibiofilm efficacy can be enhanced at lower doses [61,62].

3.6. Phytotoxicity Tests of AgNPs in Phaseolus vulgaris

AgNPs exposure produced a clear concentration-dependent response in Phaseolus vulgaris, consistent with previous reports describing stimulation at low doses and phytotoxicity at higher concentrations, affecting germination, biomass, and photosynthetic pigments [63]. In this study, low to intermediate AgNPs concentrations (5–100 µg/mL) generally supported seedling growth relative to the highest dose, whereas 500 µg/mL markedly reduced root/stem length and fresh/dry biomass (Table 3). Root length increased from 2.00 ± 0.12 cm (5 µg/mL) to 3.50 ± 0.42 cm and 3.27 ± 0.50 cm (50 and 100 µg/mL) but decreased to 1.77 ± 0.42 cm at 500 µg/mL. A similar pattern was observed for shoot length and biomass, with a pronounced reduction at 500 µg/mL, indicating growth inhibition at the highest exposure level.

Table 3. Effects of AgNPs concentrations on *Phaseolus vulgaris* growth and biomass.

AgNPs Concentrations	Control Positive	Control Negative	5 µg/mL	50 µg/mL	100 µg/mL	500 µg/mL
Root length (cm)	1.03 ± 0.01	2.93 ± 0.38	2.00 ± 0.12	3.50 ± 0.42	3.27 ± 0.50	1.77 ± 0.42
Stem length (cm)	4.50 ± 0.12	7.00 ± 0.47	6.17 ± 0.58	8.50 ± 0.82	8.83 ± 2.08	2.67 ± 0.25
Fresh weight of stems (g)	0.40 ± 0.00	0.04 ± 0.00	0.42 ± 0.01	0.42 ± 0.01	0.68 ± 0.04	0.05 ± 0.00
Fresh weight of leaves (g)	0.02 ± 0.00	0.07 ± 0.00	0.26 ± 0.00	0.30 ± 0.01	0.37 ± 0.00	0.05 ± 0.00
Fresh weight of roots (g)	0.12 ± 0.00	0.32 ± 0.00	0.05 ± 0.01	0.39 ± 0.01	0.13 ± 0.00	0.01 ± 0.00
Dry weight of stems (g)	0.01 ± 0.00	0.04 ± 0.00	0.06 ± 0.01	0.08 ± 0.01	0.07 ± 0.00	0.02 ± 0.00
Dry weight of leaves (g)	0.06 ± 0.00	0.02 ± 0.00	0.04 ± 0.00	0.05 ± 0.02	0.04 ± 0.00	0.01 ± 0.00
Dry weight of roots (g)	0.02 ± 0.00	0.01 ± 0.00	0.02 ± 0.00	0.03 ± 0.01	0.03 ± 0.00	0.001 ± 0.00
Chlorophyll a	0.21 ± 0.02	0.30 ± 0.11	0.29 ± 0.01	0.33 ± 0.02	0.83 ± 0.02	0.26 ± 0.01
Chlorophyll b	0.08 ± 0.02	0.31 ± 0.14	0.15 ± 0.02	0.20 ± 0.08	0.47 ± 0.03	0.26 ± 0.01
Total chlorophyll	0.28 ± 0.03	0.58 ± 0.26	0.45 ± 0.01	0.52 ± 0.08	1.30 ± 0.03	0.52 ± 0.02

Control negative: sterile Milli-Q water; Control positive: 0.05 M zinc sulfate heptahydrate ($ZnSO_4 \cdot 7H_2O$).

Photosynthetic pigment responses mirrored this dose dependence. Total chlorophyll increased from 0.45 ± 0.01 (5 µg/mL) to 1.30 ± 0.03 (100 µg/mL), followed by a decrease to 0.52 ± 0.02 at 500 µg/mL. This pattern is consistent with a phyto-stimulatory effect at low/moderate doses and stress-related inhibition at high doses, as described for AgNPs exposure in other plant systems [64]. The positive control produced lower chlorophyll contents than the negative control, supporting that the assay conditions were sensitive to phytotoxic stress. The effects of AgNPs exposure on seedling growth, biomass, and photosynthetic pigments in *P. vulgaris* are summarized in Table 3.

Statistical analysis supported these trends. One-way ANOVA showed a significant effect of AgNPs concentration on root length ($p < 0.0001$) and stem length ($p < 0.0001$). Tukey's test indicated no differences between 50 and 100 µg/mL for stem length ($p = 0.9866$), while the 500 µg/mL treatment showed a marked reduction relative to the other conditions, reinforcing that growth inhibition was concentrated at the highest dose.

The reduction in root growth, biomass, and chlorophyll at 500 µg/mL suggests AgNPs-induced stress, potentially linked to silver uptake and accumulation at the root surface, together with contributions from dissolved Ag^+ and associated oxidative-stress responses [65]. After root absorption, silver species can be translocated through the xylem and accumulate in tissues (cell walls and vacuoles), which may interfere with nutrient transport and photosynthetic performance [66,67]. Oxidative stress driven by reactive oxygen species overproduction has been widely proposed as a major mechanism underlying growth inhibition and pigment loss under AgNPs exposure [68,69]. Because dissolved Ag^+ release from the AgNPs suspensions was not directly quantified here, the relative contributions of ionic silver versus nanoparticle-specific interactions cannot be fully separated and should be addressed in future studies through direct Ag^+ measurements.

4. Conclusions

In this study, *Staphylococcus* sp. YRA mediated the extracellular biosynthesis of AgNPs and produced colloidal suspensions exhibiting antibacterial and antibiofilm activity against multidrug-resistant bacteria. In *Phaseolus vulgaris*, AgNPs exposure elicited a dose-dependent response, with growth stimulation at low-to-moderate concentrations and phytotoxic effects at higher doses. Together, these results support environmental *Staphylococcus* isolates as practical microbial platforms for green AgNPs production and highlight the importance of considering both antimicrobial performance and plant-related endpoints when assessing potential applications. Further work should quantify Ag^+ release and evaluate biocompatibility in relevant mammalian models to define safe use ranges.

Supplementary Materials: The following supporting information can be downloaded at: https://www.mdpi.com/article/10.3390/nano16040275/s1, Table S1: Overview of experiments, expected outcomes, and controls; Table S2: Strains included in this study (identification and key markers); Table S3: Antimicrobial susceptibility profile interpreted according to CLSI.

Author Contributions: Conceptualization, R.B.-A., Y.B.-M. and A.M.-R.; methodology, R.B.-A., Y.B.-M. and A.M.-R.; software, A.M.-R.; validation, R.B.-A., Y.B.-M. and A.M.-R.; formal analysis, R.B.-A., Y.B.-M. and A.M.-R.; investigation, Y.B.-M. and A.M.-R.; resources, R.B.-A.; data curation, Y.B.-M. and A.M.-R.; writing—original draft preparation, Y.B.-M. and A.M.-R.; writing—review and editing, R.B.-A.; visualization, Y.B.-M. and A.M.-R.; supervision, R.B.-A.; project administration, R.B.-A.; funding acquisition, R.B.-A. All authors have read and agreed to the published version of the manuscript.

Funding: This research was funded by University of Cartagena. The APC was funded by University of Sinú, Seccional Cartagena.

Data Availability Statement: The original contributions presented in this study are included in the article. Further inquiries can be directed to the corresponding authors.

Conflicts of Interest: The authors declare no conflicts of interest.

References

1. National Nanotechnology Initiative. NNI Strategic Plan 2023. Available online: https://www.nano.gov/sites/default/files/pub_resource/2023-strategic-plan.pdf (accessed on 15 December 2025).
2. Joudeh, N.; Linke, D. Nanoparticle classification, physicochemical properties, characterization, and applications: A comprehensive review for biologists. *J. Nanobiotechnol.* **2022**, *20*, 262. [CrossRef]

3. Ranjan, A.; Rajput, V.D.; Minkina, T.; Bauer, T.; Chauhan, A.; Jindal, T. Nanoparticle-induced stress and toxicity in plants. *Environ. Nanotechnol. Monit. Manag.* **2021**, *15*, 100457. [CrossRef]
4. Wang, H.; Qiao, X.; Chen, J.; Ding, S. Preparation of silver nanoparticles by chemical reduction method. *Colloids Surf. A Physicochem. Eng. Asp.* **2005**, *256*, 111–115. [CrossRef]
5. Al-Khattaf, F.S. Gold and silver nanoparticles: Green synthesis, microbes, mechanism, factors, plant disease management and environmental risks. *Saudi J. Biol. Sci.* **2021**, *28*, 3624–3631. [CrossRef] [PubMed]
6. Mustapha, T.; Misni, N.; Ithnin, N.R.; Daskum, A.M.; Unyah, N.Z. A review on plants- and microorganisms-mediated synthesis of silver nanoparticles, role of plant metabolites and applications. *Int. J. Environ. Res. Public Health* **2022**, *19*, 674. [CrossRef] [PubMed]
7. Ahmed, T.; Shahid, M.; Noman, M.; Niazi, M.B.K.; Zubair, M.; Almatroudi, A.; Li, B. Bioprospecting a native silver-resistant *Bacillus safensis* strain for green synthesis and subsequent antibacterial and anticancer activities of silver nanoparticles. *J. Adv. Res.* **2020**, *24*, 475–483. [CrossRef] [PubMed]
8. Arif, R.; Uddin, R. A review on recent developments in the biosynthesis of silver nanoparticles and its biomedical applications. *Med. Devices Sens.* **2021**, *4*, e10158. [CrossRef]
9. Aguilar-Garay, R.; Lara-Ortiz, L.F.; Campos-López, M.; Gonzalez-Rodriguez, D.E.; Gamboa-Lugo, M.M.; Mendoza-Pérez, J.A.; Anzueto-Ríos, Á.; Nicolás-Álvarez, D.E. A Comprehensive Review of Silver and Gold Nanoparticles as Effective Antibacterial Agents. *Pharmaceuticals* **2024**, *17*, 1134. [CrossRef]
10. Holubnycha, V.; Husak, Y.; Korniienko, V.; Bolshanina, S.; Tveresovska, O.; Myronov, P.; Holubnycha, M.; Butsyk, A.; Borén, T.; Banasiuk, R.; et al. Antimicrobial activity of two different types of silver nanoparticles against ESKAPE pathogens: Antibacterial and antibiofilm effects. *Nanomaterials* **2024**, *14*, 202. [CrossRef]
11. Verduzco-Chavira, K.; Vallejo-Cardona, A.A.; González-Garibay, A.S.; Torres-González, O.R.; Sánchez-Hernández, I.M.; Flores-Fernández, J.M.; Padilla-Camberos, E. Antibacterial and antibiofilm activity of chemically and biologically synthesized silver nanoparticles. *Antibiotics* **2023**, *12*, 1084. [CrossRef]
12. Li, H.; Yang, Z.; Khan, S.A.; Walsh, L.J.; Seneviratne, C.J.; Ziora, Z.M. Characteristics of Metallic Nanoparticles (Especially Silver Nanoparticles) as Anti-Biofilm Agents. *Antibiotics* **2024**, *13*, 819. [CrossRef]
13. Godakhindi, V.; Kravitz, E.; Vivero-Escoto, J.L. Light-activable silver nanoparticles for combatting antibiotic resistance in MDR bacterial infections and biofilm elimination. *Molecules* **2025**, *30*, 626. [CrossRef] [PubMed]
14. Limpiteeprakan, P.; Babel, S.; Lohwacharin, J.; Takizawa, S. Release of Silver Nanoparticles from Fabrics during the Course of Sequential Washing. *Environ. Sci. Pollut. Res.* **2016**, *23*, 22810–22818. [CrossRef] [PubMed]
15. Aslani, F.; Bagheri, S.; Muhd Julkapli, N.; Juraimi, A.S.; Hashemi, F.S.G.; Baghdadi, A. Effects of engineered nanomaterials on plant growth: An overview. *Sci. World J.* **2014**, *2014*, 641759. [CrossRef] [PubMed]
16. Tripathi, D.K.; Singh, S.; Singh, S.; Pandey, R.; Singh, V.P.; Sharma, N.C.; Chauhan, D.K. An overview on manufactured nanoparticles in plants: Uptake, translocation, accumulation and phytotoxicity. *Plant Physiol. Biochem.* **2017**, *110*, 2–12. [CrossRef]
17. Verma, D.K.; Patel, S.; Singh Kushwah, K. Green biosynthesis of silver nanoparticles and impact on growth, chlorophyll, yield and phytotoxicity of *Phaseolus vulgaris* L. *Vegetos* **2020**, *33*, 648–657. [CrossRef]
18. Baena-Baldiris, D.; Montes-Robledo, A.; Baldiris-Avila, R. *Franconibacter* 7MS: A new strain in decolorization and degradation of azo dyes ponceau S red and methyl orange. *ACS Omega* **2020**, *5*, 28146–28157. [CrossRef]
19. Whitman, W.B. (Ed.) *Bergey's Manual of Systematics of Archaea and Bacteria*; John Wiley & Sons, Inc.: Hoboken, NJ, USA, 2015. [CrossRef]
20. Weisburg, W.G.; Barns, S.M.; Pelletier, D.A.; Lane, D.J. 16S ribosomal DNA amplification for phylogenetic study. *J. Bacteriol.* **1991**, *173*, 697–703. [CrossRef]
21. Tamura, K.; Stecher, G.; Kumar, S. MEGA 12: Molecular Evolutionary Genetics Analysis Version 12. *Mol. Biol. Evol.* **2025**, *42*, msae210. [CrossRef]
22. Karthik, C.; Radha, K.V. Biosynthesis and characterization of silver nanoparticles using Enterobacter aerogenes: A kinetic approach. *Dig. J. Nanomater. Biostruct.* **2012**, *7*, 1007–1014.
23. Singh, R.; Wagh, P.; Wadhwani, S.; Gaidhani, S.; Kumbhar, A.; Bellare, J.; Chopade, B.A. Synthesis, optimization and characterization of silver nanoparticles from *Acinetobacter calcoaceticus* and their enhanced antibacterial activity when combined with antibiotics. *Int. J. Nanomed.* **2013**, *8*, 4277–4290. [CrossRef]
24. Bradford, M.M. A rapid and sensitive method for the quantitation of microgram quantities of protein utilizing the principle of protein-dye binding. *Anal. Biochem.* **1976**, *72*, 248–254. [CrossRef]
25. Singh, R.; Shedbalkar, U.U.; Nadhe, S.B.; Wadhwani, S.A.; Chopade, B.A. Lignin peroxidase mediated silver nanoparticle synthesis in *Acinetobacter* sp. *AMB Express* **2017**, *7*, 226. [CrossRef] [PubMed]
26. Khaleghi, M.; Khorrami, S.; Ravan, H. Identification of a *Bacillus thuringiensis* strain isolated from mine soil as a robust agent in the biosynthesis of silver nanoparticles with strong antibacterial and anti-biofilm activities. *Biocatal. Agric. Biotechnol.* **2019**, *18*, 101047. [CrossRef]

27. Esmail, R.; Al-Jumaili, A.; Al-Khafaji, S.; Al-Khafaji, K.; Al-Khafaji, Z.; Al-Khafaji, H. Synthesis of silver nanoparticles with high efficiency and stability by culture supernatant of Zarshouran gold mine bacteria. *BMC Microbiol.* **2022**, *22*, 97. [CrossRef] [PubMed]
28. Ghiuta, I.; Cristea, D.; Croitoru, C.; Kost, J.; Wenkert, R.; Vyrides, I.; Munteanu, D. Characterization and antimicrobial activity of silver nanoparticles biosynthesized using *Bacillus* species. *Appl. Surf. Sci.* **2018**, *438*, 66–73. [CrossRef]
29. Mehmood, A.; Ijaz, H.; Sharif, M.; Jabeen, F.; Hussain, S.; Rasool, K. Optimization and bio-fabrication of phyto-mediated silver nanoparticles: An eco-friendly approach with enhanced antimicrobial, antioxidant, and cytotoxic potential. *J. Biomol. Struct. Dyn.* **2024**, *42*, 8063–8072. [CrossRef]
30. Vogel, A.I. *Quantitative Inorganic Analysis*, 3rd ed.; Longmans: London, UK, 1961; pp. 286–288.
31. Akhatova, F.; Konnova, S.; Kryuchkova, M.; Batasheva, S.; Mazurova, K.; Vikulina, A.; Rozhina, E. Comparative characterization of iron and silver nanoparticles: Extract-stabilized and classical synthesis methods. *Int. J. Mol. Sci.* **2023**, *24*, 9274. [CrossRef]
32. Khane, Y.; Benouis, K.; Albukhaty, S.; Sulaiman, G.M.; Abomughaid, M.M.; Al Ali, A.; Aouf, D.; Fenniche, F.; Khane, S.; Chaibi, W.; et al. Green synthesis of silver nanoparticles using aqueous *Citrus limon* zest extract: Characterization and evaluation of their antioxidant and antimicrobial properties. *Nanomaterials* **2022**, *12*, 2013. [CrossRef]
33. Yotsumoto, M.; Matsuo, M.; Hishida, M.; Nakanishi, S.; Denda, M.; Nakata, S. Masking effects of odorants on a malodorous molecule in a polydopamine-modified surface: Surface zeta potential study. *Colloids Surf. A Physicochem. Eng. Asp.* **2025**, *706*, 138460. [CrossRef]
34. Afandy, H.H.; Sabir, D.K.; Aziz, S.B. Antibacterial activity of the green synthesized plasmonic silver nanoparticles with crystalline structure against Gram-positive and Gram-negative bacteria. *Nanomaterials* **2023**, *13*, 1327. [CrossRef]
35. Balouiri, M.; Sadiki, M.; Ibnsouda, S.K. Methods for in vitro evaluating antimicrobial activity: A review. *J. Pharm. Anal.* **2016**, *6*, 71–79. [CrossRef] [PubMed]
36. O'Toole, G.A.; Gibbs, K.A.; Hager, P.W.; Phibbs, P.V., Jr.; Kolter, R. The global carbon metabolism regulator Crc is a component of a signal transduction pathway required for biofilm development by *Pseudomonas aeruginosa*. *J. Bacteriol.* **2000**, *182*, 425–431. [CrossRef] [PubMed]
37. Bokranz, W.; Wang, X.; Tschäpe, H.; Römling, U. Expression of cellulose and curli fimbriae by *Escherichia coli* isolated from the gastrointestinal tract. *J. Med. Microbiol.* **2005**, *54*, 1171–1182. [CrossRef] [PubMed]
38. Stepanović, S.; Vuković, D.; Hola, V.; De Bonaventura, G.; Djukić, S.; Ćirković, I.; Ruzicka, F. Quantification of biofilm in microtiter plates: Overview of testing conditions and practical recommendations for assessment of biofilm production by *Staphylococci*. *Apmis* **2007**, *115*, 891–899. [CrossRef]
39. Baldiris, R.; Teherán, V.T.; Montes, A. Anti-biofilm activity of ibuprofen and diclofenac against some biofilm producing *Escherichia coli* and *Klebsiella pneumoniae* uropathogens. *Afr. J. Microbiol. Res.* **2016**, *10*, 1518–1527. [CrossRef]
40. Yang, X.; Ye, C.; Liu, Y.; Zhao, F. Accumulation and phytotoxicity of perfluorooctanoic acid in the model plant species *Arabidopsis thaliana*. *Environ. Pollut.* **2015**, *206*, 560–566. [CrossRef]
41. Salvatore, M.; Carafa, A.M.; Carratù, G. Assessment of heavy metals phytotoxicity using seed germination and root elongation tests: A comparison of two growth substrates. *Chemosphere* **2008**, *73*, 1461–1464. [CrossRef]
42. Naraginti, S.; Li, Y.; Li Puma, G. Photocatalytic mineralization and degradation kinetics of sulphamethoxazole and reactive red 194 over silver-zirconium co-doped titanium dioxide: Reaction mechanisms and phytotoxicity assessment. *Ecotoxicol. Environ. Saf.* **2018**, *159*, 301–309. [CrossRef]
43. López-Escamilla, A.L.; López-Herrera, M.; Loaiza-Alanís, C. Efecto de diferentes agentes gelificantes en la germinación y desarrollo in vitro de plántulas de *Echinocactus platyacanthus* Link et Otto (Cactaceae). *Polibotanica* **2016**, *42*, 153–166. [CrossRef]
44. Gupta, S.D.; Agarwal, A.; Pradhan, S. Phytostimulatory effect of silver nanoparticles (AgNPs) on rice seedling growth: An insight from antioxidative enzyme activities and gene expression patterns. *Ecotoxicol. Environ. Saf.* **2018**, *161*, 624–633. [CrossRef] [PubMed]
45. Sumanta, N.; Haque, C.I.; Nishika, J.; Suprakash, R. Spectrophotometric analysis of chlorophylls and carotenoids from commonly grown fern species by using different extracting solvents. *Res. J. Chem. Sci.* **2014**, *4*, 63–69.
46. Roy, U.; Sengupta, S.; Banerjee, P.; Das, P.; Bhowal, A.; Datta, S. Assessment of the decolourization of textile dye (Reactive Yellow) using *Pseudomonas* sp. immobilized on fly ash. *J. Environ. Manag.* **2018**, *223*, 185–195. [CrossRef] [PubMed]
47. Haq, I.; Kumari, V.; Kumar, S.; Raj, A.; Lohani, M.; Bhargava, R.N. Evaluation of the phytotoxic and genotoxic potential of pulp and paper mill effluent using *Vigna radiata* and *Allium cepa*. *Adv. Biol.* **2016**, *2016*, 5386594. [CrossRef]
48. GraphPad Software. *Prism 7 User Guide*, version 7.02; GraphPad Software, Inc.: San Diego, CA, USA, 2017.
49. Pinto, V.V.; Ferreira, M.J.; Silva, R.; Santos, H.A.; Silva, F.; Pereira, C.M. Long-term effect on the stability of silver nanoparticles in aqueous medium: Effect of the synthesis and storage conditions. *Colloids Surf. A Physicochem. Eng. Asp.* **2010**, *364*, 19–25. [CrossRef]

50. Jemel, I.; Krayem, N.; Jlidi, H.; Bacha, A.B.; Alonazi, M.; Charguia, R.; Mnif, S. Structural insights and biomedical potential of biosynthesized silver nanoparticles: Antibacterial activity, anti-biofilm and cancer cell inhibition. *PeerJ* **2025**, *13*, e19608. [CrossRef]
51. Mogole, L.; Omwoyo, W.; Viljoen, E.; Moloto, M. Green synthesis of silver nanoparticles using aqueous extract of *Citrus sinensis* peels and evaluation of their antibacterial efficacy. *Green Process. Synth.* **2021**, *10*, 851–859. [CrossRef]
52. Mfon, R.E.; Al Amri, Z. Synthesis, characterisation and zeta potential of silver nanoparticles. *Am. J. Sci. Eng. Res.* **2022**, *6*, 104.
53. Contini, C.; Hindley, J.W.; Macdonald, T.J.; Barritt, J.D.; Ces, O.; Quirke, N. Size dependency of gold nanoparticles interacting with model membranes. *Commun. Chem.* **2020**, *3*, 130. [CrossRef]
54. Menichetti, A.; Mavridi-Printezi, A.; Mordini, D.; Montalti, M. Effect of size, shape and surface functionalization on the antibacterial activity of silver nanoparticles. *J. Funct. Biomater.* **2023**, *14*, 244. [CrossRef]
55. Mathivanan, K.; Selva, R.; Uthaya Chandirika, J.; Govindarajan, R.K.; Srinivasan, R. Biologically synthesized silver nanoparticles against pathogenic bacteria. *Biocatal. Agric. Biotechnol.* **2019**, *22*, 101373. [CrossRef]
56. Fentahun, T.; Fenetahun, Y. Synthesis of silver nanoparticles using bacterial and fungal reduction methods and analytical evaluation of their physical and antimicrobial characteristics. *Pak. J. Pharm. Sci.* **2019**, *32*, 123–132. [CrossRef]
57. Vadakkan, K.; Rumjit, N.P.; Ngangbam, A.K.; Vijayanand, S.; Nedumpillil, N.K. Novel advancements in the sustainable green synthesis approach of silver nanoparticles (AgNPs) for antibacterial therapeutic applications. *Coord. Chem. Rev.* **2024**, *499*, 215528. [CrossRef]
58. Alavi, M.; Hamblin, M.R. Antibacterial silver nanoparticles: Effects on bacterial nucleic acids. *Cell. Mol. Biomed. Rep.* **2023**, *3*, 35–41. [CrossRef]
59. Qayyum, S.; Oves, M.; Khan, A.U. Obliteration of bacterial growth and biofilm through ROS level rise using zero-valent iron nanoparticles. *PLoS ONE* **2017**, *12*, e0181363. [CrossRef]
60. Soliman, M.K.Y.; Salem, S.S.; Abu-Elghait, M.; Azab, M.S. Biosynthesis of Silver and Gold Nanoparticles and Their Efficacy Towards Antibacterial, Antibiofilm, Cytotoxicity, and Antioxidant Activities. *Appl. Biochem. Biotechnol.* **2023**, *195*, 1158–1183. [CrossRef]
61. Ao, H.; Wang, D.; Ma, L.; Wang, M.; Zhang, D.; Xun, X.; Wu, X.; Zhang, M.; Zong, J. Copper-Doped Borosilicate Bioactive Glass Coating Modified Bacterial Cellulose Functional Dressing for Diabetic Ulcer. *BMEMat* **2025**, e70042. [CrossRef]
62. Joshi, A.A.; Patil, R.H. Nanoparticles targeting biofilms: A new era in combating antimicrobial resistance. *Med. Microecol.* **2025**, *17*, 100156. [CrossRef]
63. Gao, M.; Chang, J.; Wang, Z.; Zhang, H.; Wang, T. Advances in transport and toxicity of nanoparticles in plants. *J. Nanobiotechnol.* **2023**, *21*, 75. [CrossRef]
64. Kumar, S.; Masurkar, P.; Sravani, B.; Bag, D.; Sharma, K.R.; Singh, P.; Minkina, T. A review on phytotoxicity and defense mechanisms of silver nanoparticles (AgNPs) in plants. *J. Nanopart. Res.* **2023**, *25*, 54. [CrossRef]
65. Song, U.; Jun, H.; Waldman, B.; Roh, J.; Kim, Y.; Yi, J.; Lee, E.J. Functional analyses of nanoparticle toxicity: A comparative study of the effects of TiO_2 and Ag on tomatoes (*Lycopersicon esculentum*). *Ecotoxicol. Environ. Saf.* **2013**, *93*, 60–67. [CrossRef] [PubMed]
66. Wu, J.; Wang, G.; Vijver, M.G.; Bosker, T.; Peijnenburg, W.J.G.M. Foliar versus root exposure of AgNPs to lettuce: Phytotoxicity, antioxidant responses and internal translocation. *Environ. Pollut.* **2020**, *261*, 114117. [CrossRef]
67. Bao, D.; Oh, Z.G.; Chen, Z. Characterization of silver nanoparticles internalized by *Arabidopsis* plants using single-particle ICP-MS analysis. *Front. Plant Sci.* **2016**, *7*, 32. [CrossRef]
68. El-Batal, A.I.; Gharib, F.A.E.L.; Ghazi, S.M.; Hegazi, A.Z.; Hafz, A.G.M.A.E. Physiological responses of two varieties of common bean (*Phaseolus vulgaris* L.) to foliar application of silver nanoparticles. *Nanomater. Nanotechnol.* **2016**, *6*, 13. [CrossRef]
69. Siddiqi, K.S.; Husen, A. Plant response to silver nanoparticles: A critical review. *Crit. Rev. Biotechnol.* **2022**, *42*, 973–990. [CrossRef]

Disclaimer/Publisher's Note: The statements, opinions and data contained in all publications are solely those of the individual author(s) and contributor(s) and not of MDPI and/or the editor(s). MDPI and/or the editor(s) disclaim responsibility for any injury to people or property resulting from any ideas, methods, instructions or products referred to in the content.